

DM-electron scattering in materials: sum rules and heterostructures

Robert Lasenby* and Anirudh Prabhu†

Stanford Institute for Theoretical Physics, Stanford University, Stanford, CA 94305, USA

(Dated: May 17, 2022)

In recent years, a growing experimental program has begun to search for sub-GeV dark matter through its scattering with electrons. An associated theoretical challenge is to compute the dark matter scattering rate in experimental targets, and to find materials with large scattering rates. In this paper we point out that, if dark matter scatters through a mediator that couples to EM charge, then electromagnetic sum rules place limits on the achievable scattering rates. These limits serve as a useful sanity check for calculations, as well as setting a theoretical target for proposed detection methods. Motivated by this analysis, we explore how conductor-dielectric heterostructures can result in enhanced scattering rates compared to bulk conductors, for dark matter masses \lesssim MeV. These effects could be especially important in computing the scattering rates from thin-film targets, e.g. superconducting detectors such as SNSPDs, TESs or MKIDs, for which the scattering rate could be enhanced by orders of magnitude at low enough dark matter masses, as well as introducing or enhancing directional dependence.

CONTENTS

I. Introduction	1
II. Dark matter scattering	2
A. EM sum rules	2
B. Scattering rates	3
III. Material projections	4
IV. Conducting layers	6
V. Thin conducting films	7
A. Lossy dielectrics	9
B. Non-uniform geometries	9
VI. Anisotropic velocity distributions	9
VII. Other mediators	10
VIII. Discussion	12
Acknowledgments	12
A. DM scattering rate formulae	12
B. DM velocity distribution	15
C. Other EM sum rules	15
References	15

I. INTRODUCTION

There is very strong evidence that some form of non-relativistic, non-Standard-Model matter makes up most

of the universe’s matter density. While it is possible that this ‘dark matter’ (DM) only interacts gravitationally, in many theories it possesses other interactions with Standard Model (SM) particles, which may allow its detection in laboratory experiments.

For fermionic dark matter candidates, or those for which some symmetry prevents absorption, the leading interaction with an SM target is usually via scattering. An extensive experimental program searching for the scattering of heavy (\gg nucleon mass) DM particles has been in progress for decades, with the latest detectors operating at the multi-ton scale [1]. So far, no convincing DM signals have been seen, which — along with other observations — has ruled out some of the most natural models for electroweak-scale DM.

Recently, there have been efforts to extend searches for DM scattering to smaller masses ($m_{\text{DM}} \ll$ GeV). While such DM particles would be produced in too large an abundance via weak-scale thermal freeze-out [2], other early-universe production mechanisms are possible, including freeze-out via lighter mediators [3], or thermal freeze-in [4–6]. The small energy depositions arising from such scatterings mean that they would not be detectable in standard WIMP direct detection experiments. Consequently, new experiments with lower energy thresholds are required, and there has been an extensive theoretical effort to identify suitable target materials and detection strategies [7–22].

An important set of models are those in which the DM scatters through a mediator that couples to EM charge. This includes models with a ‘dark photon’ mediator, which are some of the best-motivated and least-constrained possibilities for light DM [23]. In addition, for models in which the mediator is not nucleophilic, it is often the case that electrons dominate the target response, so the scattering is very similar to that for a mediator which couples to charge. Recently, it has been emphasised [24, 25] that, for these models, the scattering rate of non-relativistic DM particles in a material is controlled by the material’s ‘energy loss function’, $\text{Im}(-\epsilon_L^{-1})$,

* rlasenby@stanford.edu

† aniprabhu@stanford.edu

where ϵ_L is the longitudinal dielectric permittivity [26]. Electromagnetism constrains the properties of this energy loss function; for example, it must satisfy ‘sum rules’ imposed by causality [27, 28], including

$$\int_0^\infty \frac{d\omega}{\omega} \text{Im} \left(\frac{-1}{\epsilon_L(\omega, k)} \right) = \frac{\pi}{2} \left(1 - \frac{1}{\epsilon_L(0, k)} \right) \quad (1)$$

for any wavenumber k . We point out that this sum rule imposes non-trivial constraints on the maximum DM scattering rate; parametrically, it shows that $\bar{\Gamma} \lesssim g_{\text{DM}}^2 g_e^2 m_{\text{DM}} v_{\text{DM}}$, where g_{DM} is the DM-mediator coupling, g_e is the electron-mediator coupling, and v_{DM} is the typical DM velocity. We derive precise bounds in Section II B.

In addition to serving as a sanity check, the sum rule constraint sets an obvious target — can we find materials which come close to saturating the achievable scattering rates? While this can be achieved with theoretically simple dielectric functions — e.g. a plasmon pole at a frequency close to the DM kinetic energy scale — finding practical materials with the appropriate properties can be difficult.

We discuss how conductor-dielectric heterostructures could enable more optimized response functions, compared to bulk materials, for DM masses \lesssim MeV. As well as analysing toy examples of periodic bulk heterostructures, we analyse the very simple system of a single conductive layer. This is the physical form taken by low-energy-threshold detectors such as transition edges sensors (TESs) [29–34], microwave kinetic inductance detectors (MKIDs) [35–37], and superconducting nanowires (SNSPDs) [38–41], and we illustrate how the scattering rates of low-mass DM in such devices may be orders of magnitude larger than a naive prediction based on the bulk material properties may suggest. While existing detectors usually have energy thresholds that are too high for such effects to be significant (e.g. the results reported in [42]), they will become important for future devices.

In addition to modifying the overall scattering rate, conductor-dielectric heterostructures also introduce preferred directions, even for isotropic constituent materials, resulting in directional dependence of the DM scattering rate. Since the DM velocity distribution at Earth is expected to be anisotropic, this leads to modulation of the DM scattering rate as the Earth rotates over the course of the day. By introducing (or, for anisotropic materials, potentially enhancing) this modulation, heterostructures could help to distinguish DM signals from other backgrounds.

We also comment on how, when the dynamics of nuclei are important, the DM scattering rate for mediators which do not couple to EM charge can exceed the sum rule bounds. This is true even for mediators which only couple to electrons. We illustrate how scattering into acoustic phonons may have significantly higher rates than into optical phonons, for mediators with couplings not precisely those of a dark photon.

II. DARK MATTER SCATTERING

Suppose that a DM state χ with mass m_χ couples to a (scalar or vector) mediator of mass m , with coupling strength g_χ . If the mediator couples to EM charges, with coupling strength g_e (i.e. $\mathcal{L} \supset g_e X_\mu (\bar{e}\gamma^\mu e - \bar{p}\gamma^\mu p)$ for its couplings to electrons and protons), then as discussed in [24, 25] the scattering rate of sufficiently light, non-relativistic DM in a material will be given by

$$\Gamma \simeq \frac{2g_\chi^2 g_e^2}{e^2} \int \frac{d^3k}{(2\pi)^3} \frac{k^2}{(k^2 + m^2)^2} \text{Im} \left(\frac{-1}{\epsilon_L(\omega_k, k)} \right) \quad (2)$$

where $\epsilon_L(\omega, k)$ is the material’s longitudinal permittivity in response to charge density perturbations with frequency ω and wavevector k , and $\omega_k = k \cdot v - k^2/(2m_\chi)$ is the energy loss corresponding to momentum transfer k from a DM particle with velocity v . The integral is over momentum transfers k such that $\omega_k \geq 0$ (we are neglecting the temperature of the medium, so up-scattering does not occur). We re-derive this result using in-medium effective propagators in Appendix A, reviewing the approximations made. Even if the mediator does not couple to SM charge, as long as the electrons dominate the material response, Eq. (2) will be a good approximation (we discuss this further in Section VII). The rate Γ in Eq. (2) corresponds to the scattering rate for a single DM particle passing through the medium — in a volume V , the total scattering rate will be given by $\Gamma_{\text{tot}} = \Gamma n_\chi V$, where n_χ is the DM number density.

A. EM sum rules

To make Eq. (2) more precise, we need to define ϵ_L more carefully. We will suppose that we have some periodic structure, and will consider its response to a small longitudinal free charge density perturbation ($\rho_f = \rho_0 e^{-i(\omega t - k \cdot x)}$, with associated current perturbation $J_f = J_0 \hat{k} e^{-i(\omega t - k \cdot x)}$, where $k J_0 = \omega \rho_0$).¹ The ‘displacement’ field is defined as $D = \hat{k} \rho_f / ik$, and the effective (inverse) permittivity is defined as the (position-dependent) linear response function for the electric field, $E_i = \epsilon_{ij}^{-1} D_j$. Then, we define the effective longitudinal dielectric function as $\epsilon_L^{-1}(\omega, k) \equiv \overline{\hat{k}_i \hat{k}_j \epsilon_{ij}^{-1}}$, where the overline denotes spatial averaging.

At high enough frequencies, faster than the response times of system’s matter, $\epsilon_L^{-1}(\omega, k) \rightarrow 1$. Consequently, via the Kramers-Kronig relations, we have

$$1 - \epsilon_L^{-1}(0, k) = \frac{2}{\pi} \int_0^\infty \frac{d\omega}{\omega} \text{Im} (-\epsilon_L^{-1}(\omega, k)) \quad (3)$$

¹ as usual, complex quantities of this kind are used as shorthand for their real parts.

(ϵ_L^{-1} is real at $\omega = 0$, since its imaginary part is an odd function of ω). There are also other sum rules [27], as reviewed in Appendix C, but this one will be most useful for our purposes. For a physical system in its ground state, we should have $\text{Im}(-\epsilon_L^{-1}(\omega)) \geq 0$ for all frequencies, corresponding to the system always absorbing (rather than emitting) energy in response to a perturbation.² So, integrating over any range of positive frequencies, we should have

$$\int \frac{d\omega}{\omega} \text{Im}(-\epsilon_L^{-1}(\omega, k)) \leq \frac{\pi}{2} (1 - \epsilon_L^{-1}(0, k)) \quad (4)$$

This lets us bound the integral over any range of ω in terms of the (inverse) static dielectric function $\epsilon_L^{-1}(0, k)$ at the appropriate k . Since $\epsilon_L^{-1}(0, k = 0)$ must be non-negative for a stable system [44], it follows by continuity that $-\epsilon_L^{-1}(0, k)$ should be small for k much less than relevant momentum scales in the system. While it is possible for $-\epsilon_L^{-1}(0, k)$ to be positive for non-zero k — indeed, this is probably the case for some metals, such as aluminium [44] — it only becomes large and positive for systems close to a point of instability, corresponding to diverging response to a charge density perturbation [44]. As a result, for most materials, the RHS of Eq. 4 will be $\mathcal{O}(1)$.

B. Scattering rates

We can use the sum-rule bound from Eq. (4) to bound the DM scattering rate in our target system. Starting from the scattering rate in Eq. (2), we want to average over DM velocities, to obtain the average scattering rate

$$\bar{\Gamma} \simeq \frac{2g_\chi^2 g_e^2}{e^2} \int \frac{d^3k}{(2\pi)^3} \frac{k^2}{(k^2 + m^2)^2} \times \int d^3v p(v) \text{Im} \left(\frac{-1}{\epsilon_L(\omega_{k,v}, k)} \right) \quad (5)$$

where $p(v)$ is the probability distribution for DM velocities.

Properly, we should consider mounting our target in a particular lab-frame orientation, and then changing this orientation relative to the Galactic frame according to the Earth's rotation. Instead, to simplify our initial calculations, we will average over *all* detector orientations relative to the Galactic frame, which can equivalently be viewed as specifying an appropriate *isotropic* $p(v)$ in Eq. (5) (we discuss anisotropic velocity distributions in Section VI). For isotropic materials, this gives the correct rate directly; for other materials, it still provides the

expected rate for a randomly-chosen orientation. In general, if we are allowed to tune the medium properties and the initial DM velocity, we can obtain arbitrarily large scattering rates, via matching the on-shell momentum transfers possible for the DM particle to the dispersion of weakly-damped excitations in the medium (so that we obtain resonant scattering at all momentum transfers). However, if we are interested in the scattering rate averaged over different directions, such tuning is no longer possible, and as we will see, it is possible to set general limits on the scattering rate.

For a given k , the frequency $\omega_{k,v} = k \cdot v - k^2/(2m_\chi)$ only depends on $|k|$ and $k \cdot v$, so it only depends on the component v_k of the velocity in the \hat{k} direction. Thus, if we write $p_1(v_k)$ as the probability distribution for the projection of the DM velocity onto a particular axis (this is independent of the axis, since we are assuming that $p(v)$ is isotropic), then

$$\bar{\Gamma} \simeq \frac{2g_\chi^2 g_e^2}{e^2} \int \frac{d^3k}{(2\pi)^3} \frac{k^2}{(k^2 + m^2)^2} \times \int_{k/(2m_\chi)}^\infty dv_k p_1(v_k) \text{Im} \left(\frac{-1}{\epsilon_L(\omega_{k,v_k}, k)} \right) \quad (6)$$

Since $d\omega_{k,v} = k dv_k$, this is equal to

$$\bar{\Gamma} = \frac{2g_\chi^2 g_e^2}{e^2} \int \frac{d^3k}{(2\pi)^3} \frac{k}{(k^2 + m^2)^2} \times \int_0^\infty d\omega p_1(v_k(\omega)) \text{Im} \left(\frac{-1}{\epsilon_L(\omega, k)} \right). \quad (7)$$

Now, we can use the sum-rule bound from Eq. (4), which implies that

$$\int_0^\infty \frac{d\omega}{\omega} \omega p_1(v_k(\omega)) \text{Im} \left(\frac{-1}{\epsilon_L(\omega, k)} \right) \leq \frac{\pi}{2} \left(1 - \frac{1}{\epsilon_L(0, k)} \right) \max_\omega (\omega p_1(v_k(\omega))) \quad (8)$$

Consequently, if we write $g_0(k) \equiv 1 - \epsilon_L^{-1}(0, k)$, then

$$\bar{\Gamma} \leq \frac{\pi g_\chi^2 g_e^2}{e^2} \int \frac{d^3k}{(2\pi)^3} \frac{k}{(k^2 + m^2)^2} g_0(k) \max_\omega (\omega p_1(v_k(\omega))) = \frac{g_\chi^2 g_e^2}{2\pi e^2} \int dk \frac{k^3}{(k^2 + m^2)^2} g_0(k) \max_\omega (\omega p_1(v_k(\omega))) \quad (9)$$

(where the $g_0(k)$ in the second line is angle-averaged). We can use an explicit form for p_1 to evaluate this expression. For an isotropic velocity distribution at a single speed v_χ , i.e. $p(v) \propto \delta(|v| - v_\chi)$, we have $p_1(v_k) = \frac{1}{2v_\chi} \mathbf{1}_{|v_k| \leq v_\chi}$, and so $\max_\omega (\omega p_1(v_k(\omega))) = \frac{k}{2} - \frac{k^2}{4m_\chi v_\chi}$ for $k \leq 2m_\chi v_\chi$. Consequently, if we have an upper bound g_0 for $g_0(k)$, then for a massless mediator ($m = 0$),

$$\bar{\Gamma} \leq \frac{g_\chi^2 g_e^2 g_0}{2\pi e^2} \int_0^{2m_\chi v_\chi} \frac{dk}{k} \left(\frac{k}{2} - \frac{k^2}{4m_\chi v_\chi} \right) = \frac{g_\chi^2 g_e^2 g_0}{4\pi e^2} m_\chi v_\chi \quad (10)$$

² this condition will not necessarily apply to a system in a metastable state, such as the ‘magnetic bubble chamber’ proposal of [43].

(if we have an explicit form for $g_0(k)$, we can use this instead). In the opposite limit, for a heavy mediator, $m \gg 2m_\chi v_\chi$,

$$\begin{aligned} \bar{\Gamma} &\leq \frac{g_\chi^2 g_e^2 g_0}{2\pi e^2} \int_0^{2m_\chi v_\chi} dk \frac{k^3}{m^4} \left(\frac{k}{2} - \frac{k^2}{4m_\chi v_\chi} \right) \\ &= \frac{g_\chi^2 g_e^2 g_0}{4\pi e^2} \frac{16}{15} m_\chi v_\chi \left(\frac{m_\chi v_\chi}{m} \right)^4 \end{aligned} \quad (11)$$

These results for a single-speed distribution can be directly applied to scattering inside a deep gravitational well, e.g. inside stars [45], where the DM velocity is close to the escape velocity. Bounds for more complicated velocity distributions can most simply be obtained by averaging over the single-speed bounds. However, this is not necessarily optimal; by using Eq. (9) with a specific p_1 directly, we can generally obtain tighter bounds. For example, using the truncated Maxwell-Boltzmann velocity distribution from Appendix B gives

$$\bar{\Gamma} \leq \bar{\Gamma}_{\text{opt}} \equiv 0.68 \times \frac{g_\chi^2 g_e^2 g_0}{4\pi e^2} m_\chi v_0 \quad (12)$$

for a massless mediator, where $v_0 \simeq 230 \text{ km s}^{-1}$ is the characteristic halo velocity scale (the escape velocity $v_{\text{esc}} \simeq 600 \text{ km s}^{-1}$ affects the 0.68 coefficient, though only weakly), and

$$\bar{\Gamma} \leq 9.1 \times \frac{g_\chi^2 g_e^2 g_0}{4\pi e^2} m_\chi v_0 \left(\frac{m_\chi v_0}{m} \right)^4 \quad (13)$$

for a heavy mediator.

We can gain some more insight into the expression in Eq. (7) by separating it into integrals over momentum and solid angle,

$$\begin{aligned} \bar{\Gamma} &\simeq \frac{2g_\chi^2 g_e^2}{e^2} \int dk \int \frac{d\omega}{\omega} \overbrace{\left[\frac{k^3 \omega}{(k^2 + m^2)^2} p_1(v_k(\omega)) \right]}^{I(\omega, k)} \\ &\times \int \frac{d\Omega_k}{(2\pi)^3} \text{Im} \left(\frac{-1}{\epsilon_L(\omega, k)} \right) \end{aligned} \quad (14)$$

Figure 1 plots the integrand term $I(\omega, k)$ for a massless mediator ($m = 0$), and p_1 corresponding to the truncated Maxwell-Boltzmann distribution from Appendix B (this will be our default p_1 going forwards). For each k , the integral is maximized by taking $\text{Im}(-\epsilon_L^{-1})$ to be a delta function at the ω which maximizes $I(\omega, k)$; as expected, this is $\omega \simeq kv_0$ for $k \lesssim m_\chi v_0$.

One important feature is that, even for a massless mediator, obtaining $\bar{\Gamma}$ of order the limit in Eq. (12) requires that most of the contribution to Eq. (14) comes from $k \sim m_\chi v_0$, $\omega \sim m_\chi v_0^2$ (assuming that $g_0(k)$ is order-1 throughout). Conversely, if we scatter entirely into excitations with energy below some threshold ω_s , where $\omega_s \ll m_\chi v_0^2$, then from Eq. (9), $\frac{\bar{\Gamma}}{\bar{\Gamma}_{\text{opt}}} \lesssim \frac{\omega_s}{m_\chi v_0^2}$.³ This illustrates that, while schemes with very low energy detection

³ This might naively seem surprising, since e.g. the Coulomb scat-

tering rate in a plasma is usually dominated by soft scatterings. However, if we are in this regime, then we can increase the scattering rate by increasing the electron density — this starts having diminishing returns once the screening scale becomes small enough, which corresponds to when soft scatterings stop dominating the rate.

Another feature to note is that, while attaining these bounds requires that $\text{Im}(-\epsilon_L^{-1})$ is concentrated at an optimum ω for each \vec{k} , as illustrated in Figure 1, taking it to be concentrated at a k -independent value ω_0 can be $\mathcal{O}(1)$ optimal. Numerically, we maximize the rate (for constant g_0) by taking $\omega_0 \simeq 0.55 m_\chi v_0^2$, which gives $\bar{\Gamma} \simeq 0.48 \times \frac{g_\chi^2 g_e^2 g_0}{4\pi e^2} m_\chi v_0$, compared to the bound in Eq. (12) which allowed the ω value to change with k .

III. MATERIAL PROJECTIONS

A wide range of papers have investigated the DM-electron scattering rates in different materials. By comparing these to the bounds derived in the previous section, we can sanity-check such calculations, as well as identifying where significant improvements might be possible.

Figure 2 compares a number of projections for different materials, in the case of a light mediator coupling to EM charge,⁴ to the bound on the per-volume scattering rate from Eq. (12). As discussed in Section II B, for sensitivity to DM masses $\sim m_0$, a material with response function concentrated around frequencies $\sim m_0 v_0^2$ is almost as good as one with an optimal response function. At frequencies $\sim 10\text{--}100 \text{ meV}$, polar materials can support optical phonon excitations, which can have $\int \frac{d\omega}{\omega} \text{Im}(-\epsilon_L^{-1})$ up to ~ 0.3 over the relevant frequency range [48] (at small k). Approximate energy-loss-function-based calculations of the DM scattering rate in such materials [49], as well as density functional theory calculations [16, 50], indicate that they are promising candidates for DM detection [16, 50–52]. The SiO₂ curves in Figure 2 illustrate that, at DM masses in the $\sim 0.1\text{--}1 \text{ MeV}$ range, the scattering rate into optical phonons can be within an order of magnitude of the sum rule bound.⁵

Other materials proposed for DM scattering experiments, such as aluminium or semiconductors, have response functions with most of their support at energies $\gtrsim 10 \text{ eV}$ [24, 25, 49], for low k . This means that their

⁴ this can be either a light dark photon mediator, or simply the SM photon itself (in the case of millicharged DM).

⁵ The SiO₂ projection in the current version (arXiv v2) of [16] corresponds to rates higher than the sum rule bound for $m_\chi \sim \text{few} \times 10^{-2} \text{ MeV}$, due to a bug in the density functional theory calculation [53], illustrating the usefulness of the sum rule bounds as a sanity check. The projections in [50] and Figure 2 [53] have been updated to correct this.

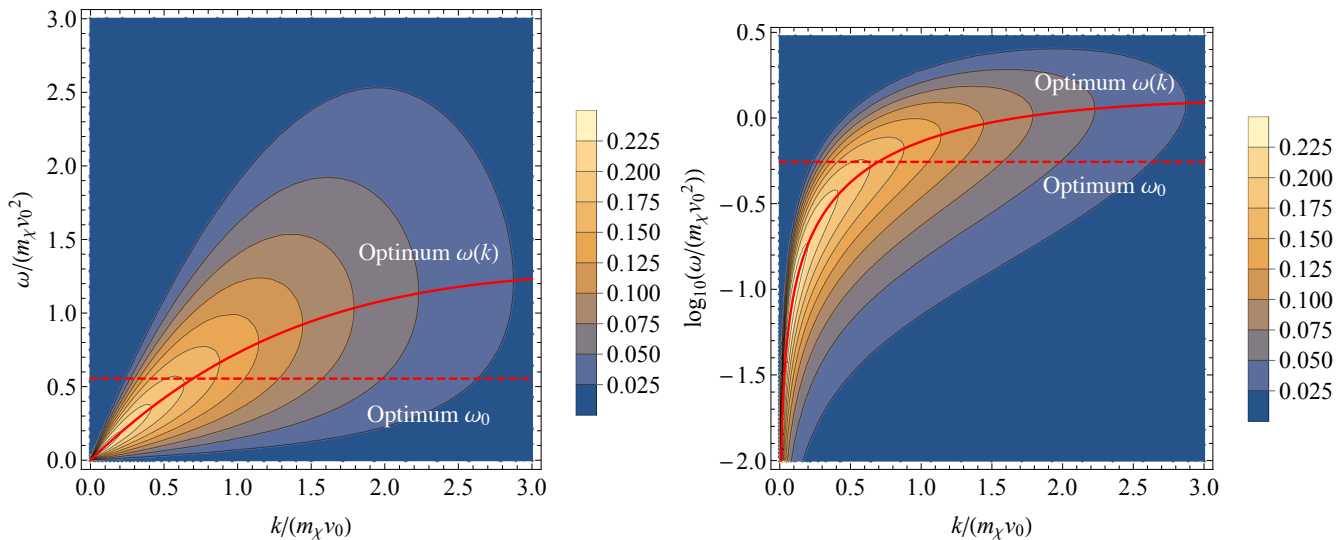


FIG. 1. *Left panel:* Integrand $I(\omega, k) = \frac{\omega}{k} p_1 \left(\frac{\omega}{k} + \frac{k}{2m_\chi} \right)$ in Eq. (14) for the DM scattering rate (with a massless mediator), taking p_1 for the truncated Maxwell-Boltzmann velocity distribution from Appendix B. Here, m_χ corresponds to the DM mass, and $v_0 = 230 \text{ km s}^{-1}$ to the characteristic velocity dispersion in the DM halo. The solid red line shows the location of the integrand's maximum for fixed k , while the dashed red line corresponds to the ω_0 such that the integral with $\omega(k) = \omega_0$ constant is largest. *Right panel:* as per left panel, but with logarithmic ω axis; the integral in Eq. (14) is with respect to $\frac{d\omega}{\omega}$, for the given integrand.

scattering rates are some way from the theoretical optimum, at all DM masses. For DM masses $\lesssim 20 \text{ MeV}$, the response function is concentrated at overly high frequencies, while for higher DM masses, the associated momentum transfers are $\gtrsim 10 \text{ keV}$, which is large enough that $\text{Im} \epsilon_L^{-1}(\omega, k)$ is significantly reduced. This is illustrated in Figure 2, which shows that the scattering rates in aluminium and silicon are always at least two orders of magnitude smaller than the volumetric optimum.⁶

The sum-rule rate in Figure 2 was obtained by setting $g_0 = 1$ in Eq. (12). This may not be precisely correct, since as discussed below Eq. (4), $g_0(k) \equiv 1 - \epsilon_L^{-1}(0, k)$ may be > 1 for large enough k . However, while we do not have full $\epsilon_L^{-1}(0, k)$ calculations or measurements for these materials, it does not seem likely that $\epsilon_L^{-1}(0, k)$ becomes large and negative — for example, the values for aluminium presented in [44] reach a minimum value of $\epsilon_L^{-1}(0, k) \simeq -0.2$ at k around half of the reciprocal lattice vector. Also, as mentioned above, $\epsilon_L^{-1}(0, k)$ should be non-negative for small enough k , so for k smaller than inverse lattice scales, $g_0 \simeq 1$ should be a good approximation. Overall, given that we are using Eq. (12) as a

parametric bound, we do not expect taking $g_0 = 1$ to be a problem.⁷

From Figure 1, we can see that, to have sensitivity to a wide range of DM masses, a material's response function should be concentrated around $\omega \simeq kv_0$. While this brings to mind the linear dispersion relations that can be realised in e.g. Dirac materials (which have been proposed as targets for DM scattering [13, 19, 21, 56]), explicit models for the permittivity in these materials, such as those given in [13, 24], do not have $\text{Im}(-\epsilon_L(\omega, k)^{-1})$ concentrated in this way.⁸

Materials with good response function support in the $\sim \text{eV}$ range may be useful for probing $\sim \text{MeV}$ mass DM. Possible examples include transparent conducting oxides [57], or non-elemental superconductors [58]. We are not aware of proper measurements of the frequency- and momentum-dependent loss function for such materials, so cannot make reliable projections. However, low-momentum measurements suggest that they may have good scattering rates. Whether excitations deposited in such materials can be reliably detected is, of course, a separate but important question.

⁶ Some earlier projections for superconducting materials, such as those in [20], did not take into account ‘screening’ effects — effectively, the $1/|\epsilon|^2$ term in $\text{Im}(-1/\epsilon) = -\text{Im}(\epsilon)/|\epsilon|^2$ — resulting in rates exceeding the sum rule bounds. What was not widely appreciated until recently [54] is that this ‘screening’ suppression also applies for a scalar mediator, as well as vector mediators. An advantage of the energy loss function formalism [24–26] is that it makes this physics transparent.

⁷ An interesting question is whether there are practical materials for which $\epsilon_L^{-1}(0, k)$ is large and negative at relevant k , so that $g_0(k) \gg 1$, and the DM scattering rate is enhanced. [44] gives the example of molten salt, which is predicted to have $\epsilon_L^{-1}(0, k) \simeq -20$ for $ka \sim \text{few}$, where a is the inter-atomic distance [55] (though such high-temperature systems are unlikely to be useful for DM detection).

⁸ The rate projections for the zero-gap model in [13] seem to be unphysically high.

Bulk materials with good response function support at very low frequencies, $\lesssim 50$ meV, are hard to achieve. However, heterostructures — structured combinations of different materials — can have different behaviour. Taking an extreme case, conducting cavities at \sim metre scales allow the low- k response function to be concentrated at \sim GHz frequencies. For DM scattering, we are interested in the response function for $k \sim 10^3\omega$ (as illustrated in Figure 1), so we need spatial structure at or below the scale k^{-1} . As we demonstrate below, straightforward combinations of conductors and insulators could allow for tailored response functions, concentrated at frequencies well below those for the bulk materials themselves.

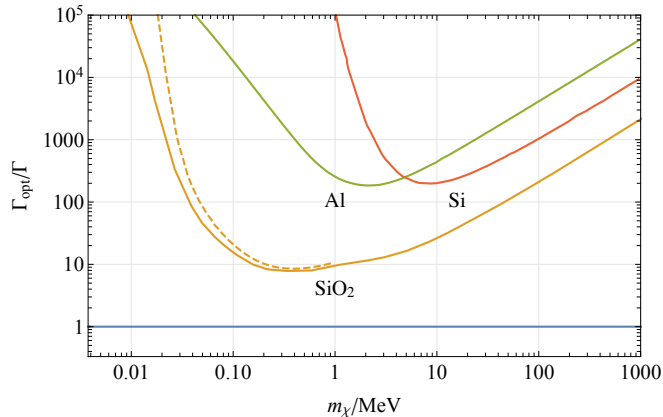


FIG. 2. Comparison of projections for DM scattering rates (via a light dark photon mediator) to the theoretical bound from Eq. (12) (taking $g_0 = 1$). The Al and Si curves correspond to the projections for electronic excitations in aluminium and silicon from [25] (see also [24]), using approximations to the energy loss function (the Al curve corresponds to an energy threshold $\omega_{\min} = 10$ meV, while the Silicon curve corresponds to excitations above the bandgap). These illustrate that the scattering rates are significantly below the theoretical optimum, especially for DM masses \ll MeV or \gg MeV. The solid SiO₂ curve corresponds to an updated [53] density functional theory projection from [16] for phonons in quartz, and the dashed curve to an energy loss function calculation from [49], illustrating that scattering into optical phonons can approach the sum rule limit more closely at suitable DM masses.

IV. CONDUCTING LAYERS

One of the simplest examples of a metal-dielectric heterostructure is an alternating array of planar layers, as illustrated in Figure 3. In response to a charge density perturbation with long wavelength (compared to the layer separation), and wavevector parallel to the planes, the effective carrier density should roughly be given by the metal's carrier density, multiplied by the volumetric filling fraction of the metal layers. Consequently, the effective plasma frequency should be decreased from its bulk value, according to the (square root of the) filling

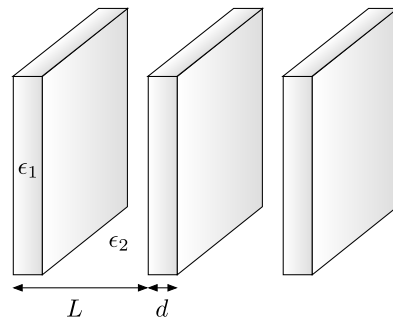


FIG. 3. Diagram of a layered heterostructure, consisting of conductive layers of thickness d and permittivity ϵ_1 , placed with spacing L in a dielectric medium of permittivity ϵ_2 .

factor. Thus, even if the metal's bulk plasma frequency is significantly larger than the DM kinetic energy scale, it may be possible to increase the scattering rate by choosing the layer thicknesses and spacings appropriately.

To analyse the response quantitatively, we will assume that we are interested in non-relativistic scatterings with $k \gg \omega$, so that magnetic fields are unimportant, and the dynamics are effectively electrostatic. For simplicity, we will take the dielectric function in each uniform medium to be isotropic and k -independent, so we want to solve $\nabla^2 \phi = -\rho_f/\epsilon_i(\omega)$, where $\rho_f = \rho_0 e^{-i(\omega t - k \cdot x)}$ as in Section II A, and ϵ_i is the dielectric function for the medium. At the medium boundaries, we need $\epsilon_1 \hat{n} \cdot \nabla \phi_1 = \epsilon_2 \hat{n} \cdot \nabla \phi_2$, where \hat{n} is the normal to the boundary, and $\phi_{1,2}$ are the solutions on each side.

Figure 3 illustrates the geometry of our setup. Taking the layers to be normal to the x direction, we can, without loss of generality, write $k = k_x \hat{x} + k_z \hat{z}$. Writing $\phi(x, z, t) = \psi(x) e^{-i(\omega t - k_x x - k_z z)}$, we want to solve for ψ . Once we have this, we can use it to compute the electric field, from which we can derive the effective longitudinal response function,

$$\overline{\hat{k} \cdot E} = \epsilon_{\text{eff},kk}^{-1} \frac{\rho_f}{ik} = \epsilon_L^{-1} \frac{\rho_f}{ik} \quad (15)$$

The general expression for ϵ_L^{-1} is rather complicated. However, in the $d/L \ll 1$ limit, where d is the width of the ϵ_1 layers and $L - d$ the width of the ϵ_2 layers, it has the simple form

$$\epsilon_L^{-1}(\omega, k) \simeq \frac{(1 - \frac{d}{L})\epsilon_1 + \frac{d}{L}\epsilon_2}{\epsilon_1\epsilon_2 + (1 - \frac{d}{L})\frac{d}{L}(\epsilon_1 - \epsilon_2)^2 \frac{k_z^2}{k^2}} \quad (16)$$

(where ϵ_1 and ϵ_2 are in general functions of ω and k). For $k_z = 0$, this is simply the volume-weighted sum of ϵ_1^{-1} and ϵ_2^{-1} , as we would expect. However, for $k_z \neq 0$, the behaviour can be significantly different (if $k_x = 0$, we have $\epsilon_L^{-1} = (\frac{d}{L}\epsilon_1 + (1 - \frac{d}{L})\epsilon_2)^{-1}$). In particular, the response poles will be at different frequencies.

If we take the limit $d/L \ll 1$, then the denominator of Eq. (16) vanishes when $\epsilon_1 \simeq -\epsilon_2 \frac{k_z^2 d}{k^2 L}$, or $\epsilon_1 \simeq -\epsilon_2 \frac{k_z^2 L}{k^2 d}$. For example, if we take a simple Drude model, $\epsilon_1 \simeq 1 -$

ω_p^2/ω^2 , then the latter equality occurs for $\omega^2 \simeq \frac{1}{\epsilon_0} \frac{k_z^2}{k^2} \frac{d}{L} \omega_p^2$. This corresponds to the expected result that the effective plasma frequency (squared) is suppressed by the filling fraction of the metal.

Consequently, compared to a bulk conductor, a heterostructure of conductor-dielectric layers will have its energy loss function concentrated at lower frequencies, so can have better sensitivity to low-mass dark matter. In Figure 4, we illustrate this with a toy example, taking the bulk conductor to have a Drude-model permittivity, $\epsilon(\omega) = \epsilon_\infty \left(1 - \frac{\omega_p^2}{\omega(\omega + i\gamma)}\right)$, where we take $\epsilon_\infty = 10$, $\omega_p = 0.5 \text{ eV}$, and $\gamma = 0.1\omega_p$ (this is in rough analogy to the optical response function for NbN [59]). Taking the DM to couple through a massless (or sufficiently low-mass) dark photon mediator, the dark red curve shows the background-free sensitivity reach for a $(2 \text{ mm})^3$ bulk volume of this material with a one-year exposure. The lighter red curve shows the sensitivity reach for the same volume of a conductor-dielectric heterostructure, where we take the conductive layer thicknesses to be $d = 1 \text{ nm}$, and the dielectric ($\epsilon = 1$) layer thicknesses to be $L - d = 4 \text{ nm}$. As expected, the layered material has better sensitivity at small DM masses, compared to an equivalent volume of the bulk conductor, and worse sensitivity at larger DM masses.

Especially at high DM masses, our toy model calculation will not be realistic. For $m_\chi \gtrsim \text{MeV}$, the characteristic momentum scale is $m_\chi v_0 \gtrsim 770 \text{ eV} = \frac{2\pi}{1.6 \text{ nm}}$, which is close enough to atomic lattice scales that the dielectric function will have non-negligible momentum dependence [25, 49]. However, for $m_\chi \lesssim \text{MeV}$, our calculations illustrate the kind of behaviour expected.

Layered structures represent only one possible kind of heterostructure. Other examples include conductor-dielectric mixtures with random structures [60], or granular inclusions (such as granular aluminium [61], which is superconducting for small enough grain separations). We leave investigation of such possibilities to future work.

V. THIN CONDUCTING FILMS

Volume-filling heterostructures, such as the layered materials considered in the previous subsection, may be an interesting option for DM scattering experiments. However, whether such materials can be constructed, and whether excitations deposited in them can be detected, are topics for future research. Nevertheless, similar calculations apply to a more concrete prospect — detection of DM scattering in superconducting thin-film detectors themselves.

Detectors for low-energy-threshold excitations, such as TESs, MKIDs, and SNSPDs, often taken the form of thin, superconducting layers. In [20], DM scattering in SNSPDs was considered, but their scattering rate was based on bulk scattering rate in the conductive material. Here, we point out that, for momentum transfers smaller

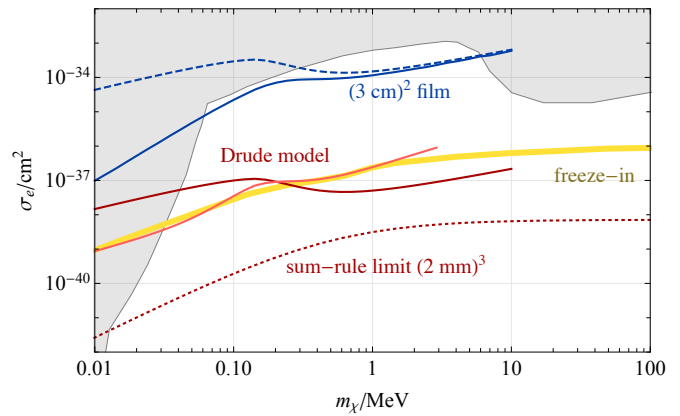


FIG. 4. Plot of DM-electron scattering cross section sensitivity versus DM mass, assuming the DM couples through a low-mass dark photon mediator. The gray shaded area shows the existing constraints [62–65], while the yellow band shows the parameters for which early-universe freeze-in [5] gives the correct DM abundance, assuming no pre-existing hidden sector population. The red curves correspond to the background-free sensitivity reach for a 1-year exposure with a $(2 \text{ mm})^3$ target volume (the sensitivity reach is taken to be the cross section that would result in 3 expected events during the exposure). The dotted red curve corresponds to the theoretical section limit from Eq. (12). The dark red curve corresponds to a bulk material target, with Drude model permittivity as described in Section IV. The lighter red curve corresponds to a layered material, with $d = 1 \text{ nm}$ thick layers of this material, alternating with $L - d = 4 \text{ nm}$ thick dielectric ($\epsilon = 1$) layers. As the plot shows, this has worse sensitivity at larger DM masses, but better sensitivity at smaller masses. The blue curve corresponds to the sensitivity reach (for a background-free 1-year exposure) from a 3 nm layer of material with area $(3 \text{ cm})^2$, for the same Drude model permittivity (taking an energy threshold $\omega_{\text{min}} = 1 \text{ meV}$). The dashed blue curve shows the sensitivity reach from an equivalent bulk volume of the same material, showing how, at low DM masses, taking into account the geometrical effects of the thin layer is very important.

than the inverse thickness scale of the film, the geometrical structure of the substrate-film-air system needs to be taken into account. Since typical film thickness are a few nm, these effects are important for $m_\chi \lesssim \text{MeV}$.⁹

For simplicity, we first analyse the case of a single, infinite layer with thickness d and permittivity ϵ , surrounded by a medium of unit permittivity. Since the thickness is finite, instead of the per-volume scattering rate being set by $\text{Im}(-\epsilon_L^{-1})$, the per-area scattering rate is set by $\text{Im}(R)$, where R is the appropriate response

⁹ For absorption of light bosonic DM, as opposed to DM scattering, the typical momentum transfer is $\sim m_{\text{DM}} v_0$, which is much less than the energy transfer $\sim m_{\text{DM}}$. Consequently, for comparable energy depositions, geometrical effects will be more important for DM absorption; for example, the bulk-material-based calculations in [20] will be modified, as mentioned in [42].

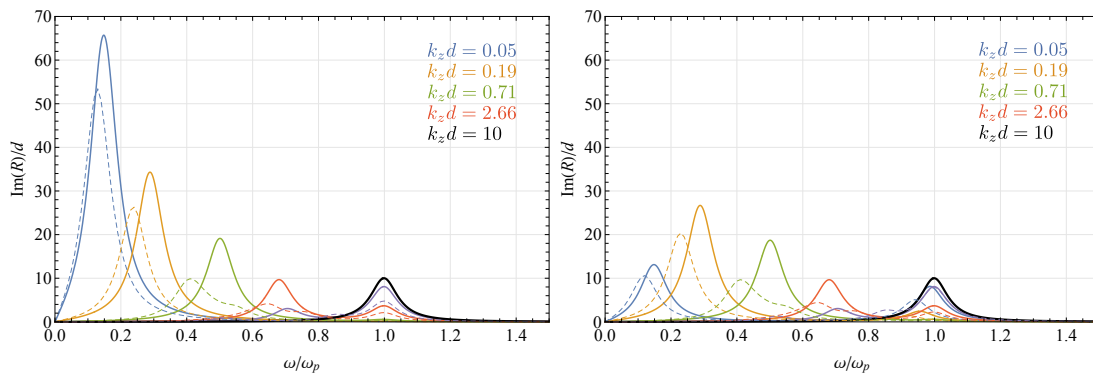


FIG. 5. *Left panel*: the solid curves show the thin-layer response function R from Eq. (19), taking a Drude model dielectric function $\epsilon = 1 - \frac{\omega_p^2}{\omega(\omega + 0.1i\omega_p)}$ and $k_x = 0$, for $k_z d$ values from 0.05 to 10. The black curve corresponds to the response function for an equivalent volume of bulk material. The dashed curves corresponds to the response for the rectangular wire geometry diagrammed in Figure 6, with $w = 6d$ and $h = 10d$. *Right panel*: as per left panel, but taking $k_x d = 0.1$.

function with dimensions of length. The time-averaged power absorbed from a longitudinal free charge perturbation J_f is $\langle P \rangle = \langle \int dV E \cdot J_f \rangle$, where E is the electric field response, and angle brackets denote time averaging. Assuming that the response is effectively electrostatic, and writing $E = -\nabla\phi = ((-\psi' + ik_x\psi)\hat{x} + ik_z\psi\hat{z})e^{-i(\omega t - k \cdot x)}$ as above (taking the layer to be normal to the x direction), we have

$$\langle P \rangle = -\frac{1}{2} \int dV \frac{\omega}{k^2} \text{Re} [\rho_0^* (ik^2\psi + k_x\psi')] \quad (17)$$

$$\equiv \frac{1}{2} A \frac{\omega}{k^2} |\rho_0|^2 \text{Im}(R) \quad (18)$$

where A is the area we are considering. For comparison, in a bulk material, we have $P = \frac{1}{2} V \frac{\omega}{k^2} |\rho_0|^2 \text{Im}(-\epsilon_L^{-1})$.

The general expression for R is somewhat complicated, but if we consider an excitation with $k \parallel \hat{z}$, then

$$R = \frac{1}{k\epsilon} \frac{2 - kd \coth(kd/2) + \epsilon(2\epsilon - 4 - kd)}{\coth(kd/2) + \epsilon} \quad (19)$$

The denominator vanishes when $\epsilon = -\coth(kd/2)$. For a simple Drude model, $\epsilon(\omega) = 1 - \omega_p^2/\omega^2$, so for $kd \ll 1$, this corresponds to a resonant frequency of $\omega^2 \simeq \frac{kd}{2}\omega_p^2$. Intuitively, the relevant filling fraction is the ratio of the layer thickness to the scattering wavelength. There is also a divergence at $\epsilon = 0$, corresponding to the bulk material resonance, but the contribution of this is suppressed for $kd \ll 1$, since $\frac{2 - kd \coth(kd/2)}{\coth(kd/2)} = -\frac{(kd)^3}{12} + \mathcal{O}((kd)^5)$. When $kd \gg 1$, we have $R \simeq -d/\epsilon$, so $\text{Im}(R) = d \text{Im}(-\epsilon^{-1})$, as expected.

As well as moving the response to lower frequencies, the $kd \ll 1$ regime can also increase the frequency-integrated response. For example, suppose that we work in an approximation where $\epsilon \rightarrow \epsilon_\infty > 1$ as $\omega \rightarrow \infty$.¹⁰

Then, for a bulk material, we have $\int \frac{d\omega}{\omega} \text{Im}(-\epsilon_L^{-1}) \leq \frac{\pi}{2} \epsilon_\infty^{-1} (1 - \epsilon_L^{-1}(0, k))$, so the frequency-averaged absorption is suppressed by ϵ_∞^{-1} . However, for the thin layer, we have

$$\int_0^\infty \frac{d\omega}{\omega} \text{Im} R(\omega) \simeq \frac{\pi}{2} k^{-1} \quad (20)$$

for $dk \ll 1$. As well as being enhanced over the equivalent volume of an ideal bulk material by $1/(dk)$, this is not suppressed by ϵ_∞^{-1} (intuitively, this occurs because the response is spread across a full wavelength around the layer, most of which is in vacuum).

These features are illustrated in the left panel of Figure 5, which plots $\text{Im} R(\omega)$ for a simple Drude-model dielectric function, at different k values. At large kd , the response is almost the same as for a bulk material, while for small kd , it is moved to lower frequencies and enhanced.

The above formulae applied to the $k_x = 0$ case. If we take the opposite limit, $k \parallel \hat{x}$, then we just have the usual bulk material response, $R = -d/\epsilon$. For intermediate directions, we interpolate between these two extremes, as illustrated in the right-hand panel of Figure 5.

The geometric effects discussed above can have important consequences for the scattering rate of low-mass DM. As illustrated in Figure 5, the shift of the $\text{Im} R(\omega)$ distribution to lower frequencies means that a thin layer can have a larger total scattering rate for low-mass dark matter than a thicker layer, even if the latter has larger volume. In Figure 4, the blue curve corresponds the sensitivity reach for scattering from a 3 nm thick film with area

good approximation if e.g. there are some effectively-decoupled, higher-frequency dynamics which contribute a background permittivity ϵ_∞ . For example, the optical energy loss function for SiO_2 has features below ~ 200 meV, corresponding to phonon dynamics, but then most of the $\int \frac{d\omega}{\omega} \text{Im}(-\epsilon_L^{-1})$ integral comes from electronic excitations at $\omega \gtrsim 10$ eV [48].

¹⁰ This will not be true in a strict physical sense, but can be a

$(3 \text{ cm})^2$, assuming a background-free exposure of 1 year. We take the Drude-model permittivity from the previous subsection, and for extra realism, assume that the layer is mounted on a dielectric substrate with permittivity $\epsilon = 11$ (corresponding to that of silica). The dotted blue curve corresponds to the sensitivity for the equivalent bulk volume of conductor. For large DM masses, $\gtrsim \text{MeV}$, the geometric effects are only $\mathcal{O}(1)$. However, for smaller masses, they can increase the scattering rate by orders of magnitude.

It should be emphasised that the calculations presented here apply to toy models. To calculate limits or sensitivity projections for actual devices, more realistic models of the materials' dielectric functions would be required — ideally, derived from actual measurements of such devices.¹¹ Similarly, the detectability of excitations absorbed in this way would need to be quantified. [42], which appeared on arXiv simultaneously with this paper, uses techniques from this paper, and data from the tungsten silicide SNSPD used in the LAMPOST dark photon DM detection experiment [67] to estimate limits on dark matter scattering with electrons, as well as making projections for future SNSPD experiments. They find that the energy threshold for this SNSPD is too high for geometrical effects to be important in DM scattering, but that these should be significant for future generations of SNSPDs (for dark photon absorption within the SNSPD, which [42] also estimates, geometric effects will be more important, as per Footnote 9).

A. Lossy dielectrics

If a thin film is not surrounded by vacuum (e.g. it is mounted on a substrate), then the surrounding dielectric will have some imaginary part to its permittivity. If we naively integrate over the entire spatial volume, this may result in the absorbed power being dominated by the bulk absorption in the dielectric.

Because of how thin-film detectors such as SNSPDs operate, we are interested in the rate of scatterings which deposit enough energy *into the conductor*, quickly enough, to register as an excitation [68]. Depending on the transport properties of energy deposited in the dielectric material, this rate may actually be dominated by bulk absorption in the dielectric. For example, this is the design principle behind detectors based on exciting optical phonons in polar crystals [69, 70] — the idea is that such excitations decay into non-thermal quasi-particles, which then propagate until they are absorbed by a superconducting detector.

To be conservative, we can restrict ourselves to excitations where the energy is directly deposited in the

conductor itself. To do so, we can calculate the electric potential response ψ , as per above, and calculate how much energy is dissipated inside the conductor given this response. If the dielectric within $\sim k^{-1}$ of the conductor is not very lossy, then this will be dominated by the conductor, giving a result analogous the lossless-dielectric case considered above. These considerations will also apply to the absorption of light bosonic DM, mentioned in footnote 6.

B. Non-uniform geometries

The calculations above assumed an infinite, uniform conductive plane. This can be a good approximation when the inverse momentum transfer is much smaller than geometric features other than the thickness of the film. However, some types of thin film detectors have transverse structure on small scales. For examples, SNSPDs [39, 71, 72] use a wire meander with small width (10s to 100s of nm), as illustrated in Figure 6, so for momentum transfers $\lesssim 0.1 \text{ keV}$, we might expect this structure to have some effects on scattering rates.

To estimate these effects, we can solve for the 2D electrostatic response across the wire's cross-section (the meander length is generally long enough that end effects are unimportant). Similarly to the 1D case, we want to solve the Poisson equation, $\nabla \cdot (\epsilon \nabla \phi) = -\rho$, with $\phi(x, y, z, t) = \psi(x, y) e^{-i(\omega t - k \cdot x)}$. Since doing this analytically is somewhat difficult for general geometries, we can instead discretise it on a 2D grid, and solve the resulting system of equations numerically to obtain ψ .

The simplest way to do this is to impose periodic boundary conditions, which means that we are effectively solving for the response of a series of equally-spaced, infinitely-long wires. The corresponding two-dimensional cross-section is shown in the lower panel of Figure 6, and some example numerical solutions for $\psi(x, y)$ are shown in Figure 7. The latter illustrate that, for $k \gtrsim d^{-1}$, the response is dominantly contained within the conductor, while for $k \ll d^{-1}$, the response extends over a range $\sim 1/k$, and approximates that from a uniform layer. The dashed curves in Figure 5 compare the numerical scattering rates derived from these ψ solutions to the analytic rates for an equivalent uniform film, illustrating that these match well at $k \ll d^{-1}$, while being volumetrically suppressed at larger k .

VI. ANISOTROPIC VELOCITY DISTRIBUTIONS

In our calculations so far, we have adopted the approximation of an isotropic DM velocity distribution. However, it is expected that, due to the velocity of the Earth with respect to the Galactic frame, the DM velocity distribution in the laboratory will be significantly anisotropic (c.f. Appendix B).

¹¹ This is especially important since, for such thin layers, one might expect the response function to differ quite significantly from that of a bulk material, due to surface effects [66].

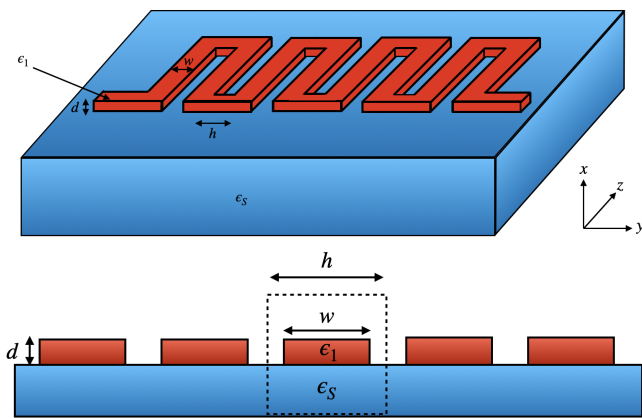


FIG. 6. *Top*: schematic of an superconducting nanowire single-photon detector (SNSPD) consisting of a superconducting wire meander (red) deposited on an electrically insulating substrate (blue). *Bottom*: two-dimensional cross section (fixed z) of the SNSPD.

Since the direction of this anisotropy in the lab frame will vary over each day as the Earth rotates, a detector for which the scattering rate depends on the direction of the incoming DM will see a daily modulation in scattering rate. The conductor-dielectric heterostructures we have been considering do have anisotropic structures, so even in the approximation where the individual materials have isotropic response functions, the overall scattering rate will still depend on the DM direction.

For the truncated Maxwell-Boltzmann distribution described in Appendix B, and considering a thin-film detector with the parameters given in Section V, Figure 8 shows the ratio of the DM scattering rates for the extreme cases of the velocity offset being parallel and perpendicular to the film (other directions give intermediate rates). For a light mediator, the effect on the overall scattering rate is $\lesssim 10\%$. Roughly speaking, this is because the phase space volume of mostly-parallel momentum transfers (which maximize collective effects) is larger for parallel DM velocities, but sits at smaller k for perpendicular DM velocities. Since small- k scatterings are enhanced for a light mediator, these effects partially cancel out, reducing the difference between perpendicular and parallel DM velocities. For heavy mediators, the ratio can be $\gtrsim 25\%$.

More complicated geometries, which modify the k -dependence of the structure's response, can also enhance the ratio between scattering rates for different DM directions. For example, in the 'SNSPD' geometry considered in Section VB, the wire width w provides an additional scale. Numerical calculations, of the kind illustrated in Figure 7, indicate that this could significantly increase the directional dependence (integrating over the full velocity distribution to obtain the analogue of Figure 8 would be possible, but computationally expensive — we leave detailed investigations to future work).

It should be emphasised that the specific calculations

described above assume that the conductor and dielectric materials both have isotropic and k -independent ϵ . For large enough frequencies and momentum transfers, this will be a poor approximation. In addition, for thin enough layers, edge effects may become important, even for materials with fairly isotropic bulk permittivities, complicating matters still further. As a result, Figure 8 should not be taken as a realistic prediction of daily modulation amplitudes. However, it does illustrate that the geometrical properties of heterostructures can lead to significant directional dependence, even in situations where the bulk material properties would not do so. This could help to distinguish a dark matter signal from laboratory backgrounds.

As well as daily modulation due to the rotation of the Earth, there is also an annual effect caused by the Earth's changing velocity around the Sun. This leads to the Earth's velocity relative to the Galactic frame changing by $\sim 60 \text{ km s}^{-1}$ over the course of the year, with the RMS DM speed varying by $\sim 3\%$. For a light mediator, this generally leads to small (percent-level) differences in the scattering rate, with larger ($\mathcal{O}(10\%)$) differences for a heavy mediator.

VII. OTHER MEDIATORS

As mentioned above, the $\text{Im}(-\epsilon_L^{-1})$ prescription, and the associated sum rules, apply in the case of a mediator that couples to EM charge. For mediators with different SM couplings, we need to consider the in-medium self-energy of that mediator, rather than the SM photon, as outlined in Appendix A.

In many circumstances, for light DM with a mediator that is not nucleophilic, the material's response is dominated by the more mobile electrons, and the $\text{Im}(-\epsilon_L^{-1})$ formulae give approximately the right results. This is true for most excitations at frequencies $\gtrsim \text{eV}$. However, for excitations in which nuclei play a significant part, such as phonons, this will no longer be the case. In particular, scattering into such excitations can violate the sum rule bounds, and allow larger rates than those for a dark photon mediator.

As an example, we can consider DM scattering via a scalar mediator which couples to electrons, but not to nucleons. For momentum transfers small enough compared to the material's inverse lattice scale, the mediator's effect will correspond to a coherent forcing, and we can excite acoustic phonons, rather than just optical phonons. If the material's sound speed is large enough, then the enhancement due to the coherent coupling to acoustic phonons can be greater than the suppression due to the velocity mismatch between acoustic phonons and typical DM velocities. Consequently, acoustic phonons can dominate the scattering rate.

This case was analysed in [18, 70]; in particular, [18] performed a density functional theory calculation for the scattering rate in GaAs, plotted in Figure 9. While this

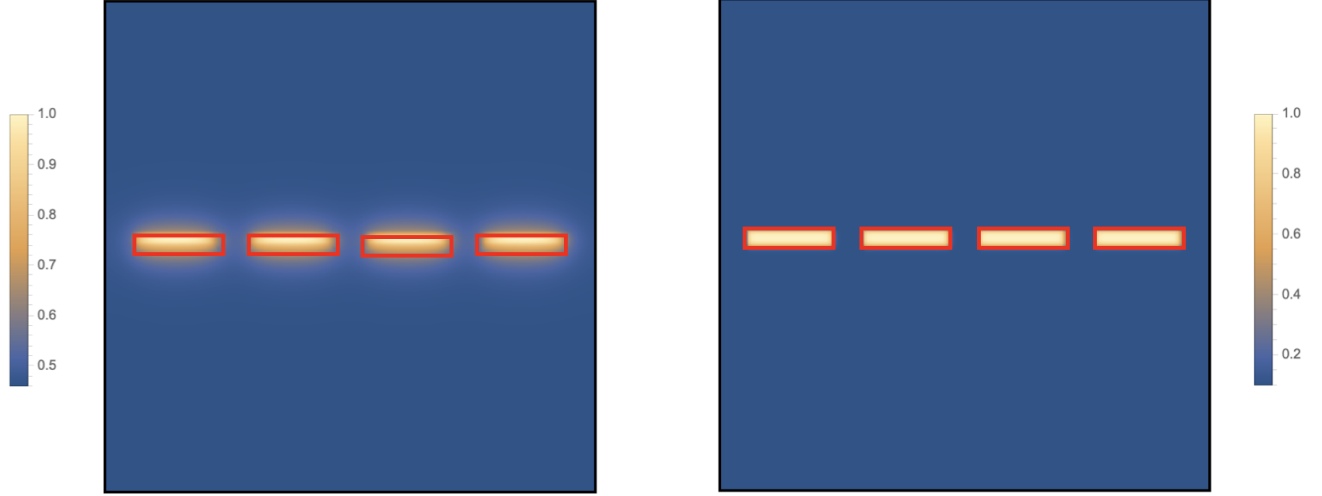


FIG. 7. Numerical solution for the response function $\psi(x, y)$, discussed in Sec. VB for a periodic array of rectangular cross-section wires (depicted by red rectangles) and $k_z d = 1$ (left panel), $k_z d = 10$ (right panel), where d is the wire thickness. Orange corresponds to higher magnitudes for ψ , and blue to smaller magnitudes (color bars are in arbitrary units).

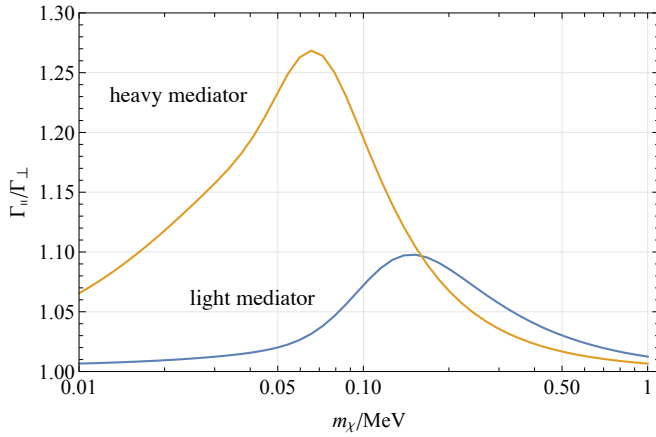


FIG. 8. Ratio of velocity-averaged scattering rates for a thin film (with properties as in Figure 4), given a truncated Maxwell-Boltzmann DM velocity distribution (Appendix B), where Γ_{\parallel} corresponds to the average DM velocity being parallel to the film, versus perpendicular to the film for Γ_{\perp} (we take an energy threshold $\omega_{\min} = 1$ meV). The blue curve assumes a light mediator, with mass much smaller than relevant momentum transfer scales, while the orange curve assumes a heavy mediator, with mass much larger than relevant momentum transfer scales.

calculation did not take into account screening, the scattering rate was dominated by acoustic phonons at small DM masses, for which screening should not be an important effect. As Figure 9 shows, the scattering rate is orders of magnitude below the sum rule limit for a mediator coupling to charge, illustrating how these limits do not apply for other types of coupling. To obtain other examples, we can translate the scattering rates for a nucleophilic scalar mediator calculated in [16]; at small

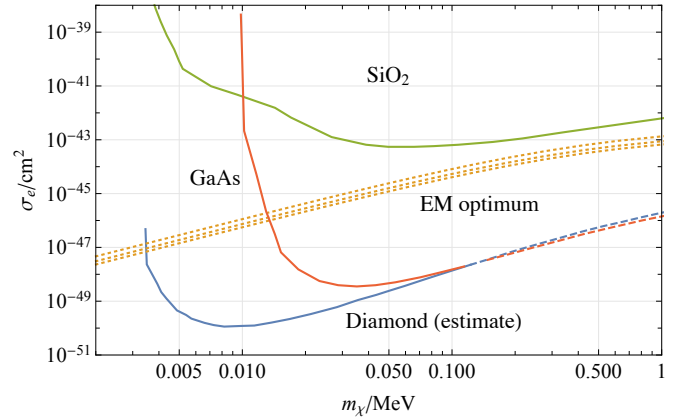


FIG. 9. Plot of sensitivity estimates for a kg-year background-free exposure (i.e. the cross section corresponding to 3 expected events), for different mediator couplings (taking an energy threshold $\omega_{\min} = 1$ meV). The red curve shows the calculation for GaAs with a leptophilic scalar mediator from [18] (the higher-DM-mass part of this curve is shown dashed, since neglected effects such as screening should be least important at small DM masses, where acoustic phonons dominate the rate). The blue curve shows the estimated rate for scattering in diamond via a leptophilic mediator, based on the nucleophilic mediator result from [16]. The green curve shows an updated [53] density functional theory projection from [16] for phonons in SiO_2 , assuming a light mediator coupling to EM charge. The orange dotted lines shows the optimum sensitivity for a mediator coupling to charge (the upper line corresponds to the density of GaAs, the middle line to the density of diamond, and the lower line to the density of SiO_2).

enough momentum transfers, the coupling of a leptophilic mediator to acoustic phonons can be related to that of a nucleophilic mediator by comparing the nucleon density

to the electron density. Figure 9 shows this translation for the diamond calculation from [16], illustrating how diamond’s faster sound speed results in larger scattering rates for small DM masses.

Even for a scalar mediator with equal and opposite couplings to electrons and protons, the different velocities of electrons and protons in materials will mean that it has some non-zero coupling to neutral bulk matter. Consequently, it can couple coherently to acoustic phonons. Given that un-suppressed couplings to acoustic phonons can result in very large scattering rates (c.f. Figure 9), we might wonder whether corrections suppressed by the SM fermion velocities could dominate the scattering rate at low DM masses, even for a scalar mediator coupling to charge. To estimate this, we can note that $\bar{f}\gamma^0 f \simeq (1 + v^2/2)\bar{f}f$ for a non-relativistic fermion. Typical inner-shell electron velocities are $\sim Z\alpha$, while proton velocities in nuclei are $\mathcal{O}(0.1)$. As a result, we expect typical deviations from bulk neutrality at the $\mathcal{O}(10^{-2})$ level, with the consequence that scattering into acoustic phonons may well be important for low-mass DM. Of course, it is difficult for DM models with a non-nucleophilic scalar mediator to account for all of dark matter without running into other constraints [23], and for a small enough dark matter sub-component, even the scattering rates possible with a leptophilic mediator are somewhat hard to probe experimentally [18], given existing bounds. Consequently, models where the scattering rate is further suppressed, such as a scalar mediator coupling to charge, would be even harder to see.

VIII. DISCUSSION

In this paper, we have discussed two main topics; how electromagnetic sum rules place bounds on the DM-electron scattering rate in materials, and how conductor-dielectric heterostructures can increase the scattering rate of low-mass DM, relative to bulk conductors.

To detect DM, there must be a high enough DM-target scattering rate, and we must be able to detect scatterings that occur. In most of this paper, we have focussed on the first requirement, but the second is also crucial. The very simplest way to ensure detection is for scatterings to deposit energy in the detector material itself. We have pointed out that, for thin-film superconducting detectors, which are one of the most promising routes towards low energy thresholds, geometric effects analogous to those for periodic metal-dielectric heterostructures can have a significant impact on the scattering rate for low-mass DM.

To achieve sensitivity to smaller DM couplings, volume-filling targets will be required, and further work would be needed to establish whether heterostructures could be practically useful. In particular, whether suitable materials could be manufactured, and whether excitations deposited in such materials could be reliably detected, are not obvious.

As mentioned in footnote 7, an interesting question is whether materials with large and negative (inverse) static dielectric function $\epsilon_L^{-1}(0, k)$, which have larger frequency-integrated energy loss functions, could be useful for DM detection. The most obvious examples of such systems, such as materials near the threshold of crystallisation, are high-temperature systems that are not suitable for detecting small energy depositions. We leave the investigation of possible alternatives to future work.

Beyond applications to DM detection experiments in the laboratory, our sum rule analyses may also point to other areas in which DM-SM scattering rate calculations need revision. For example, many papers have attempted to calculate the scattering rate for DM passing through the dense interiors of neutron stars or white dwarfs (see [73–75] and references therein). However, while such calculations included Pauli blocking, they did not include in-medium effects such as screening. For appropriate mediators, and sufficiently light DM, these may significantly affect the scattering rate. As an example, if we consider a heavy dark photon mediator, then the appropriate sum rule limit for the DM scattering rate is significantly lower than both the electron and nucleon scattering rates given in [75] for a white dwarf core, for dark matter masses \lesssim MeV. These topics are explored in [45].

ACKNOWLEDGMENTS

We thank Karl Berggren, Yonit Hochberg, Simon Knapen, Tongyan Lin, Tanner Trickle, and Zhengkang Zhang for helpful conversations, and Yonit Hochberg, Simon Knapen, Tongyan Lin and Zhengkang Zhang for comments on drafts. RL’s research is supported in part by the National Science Foundation under Grant No. PHYS-2014215, and the Gordon and Betty Moore Foundation Grant GBMF7946. RL thanks the Caltech physics department for hospitality during the completion of this work. AP’s research is supported by National Science Foundation under Grant No. PHYS-1720397 and the Gordon and Betty Moore Foundation Grant GBMF7946. AP acknowledges the support of the Fletcher Jones Foundation and the National Science Foundation (NSF) Graduate Research Fellowship Program.

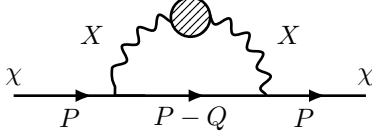
Appendix A: DM scattering rate formulae

In this appendix, we will give a condensed derivation of the DM scattering rate formula in Eq. (2), explaining the approximations being made.

1. Vector mediator

For concreteness, we will start by considering the case of a DM fermion χ , interacting with a vector mediator X_μ , with coupling $g_\chi X_\mu \bar{\chi} \gamma^\mu \chi$.

To evaluate the interaction rate of a DM fermion travelling through a medium, we can compute the fermion's in-medium self-energy. At leading order in g_χ , this is given by the imaginary part of the following diagram



where the dashed circle represents the SM medium effects. In the notation of [76], the cut self-energy is

$$\Sigma^>(P) = g_\chi^2 \int \frac{d^4 Q}{(2\pi)^4} \gamma^\mu S_0^{>F}(P-Q) \gamma^\nu D_{\mu\nu}^>(Q) \quad (\text{A1})$$

where $S_0^{>F}$ is the cut propagator for χ (in vacuum, since we assume that χ is weakly coupled and its density is low), and $D_{\mu\nu}^>$ is the in-medium cut propagator for the mediator. Using the $S_0^{>F}$ expression for a Dirac fermion, this is.

$$\Sigma^>(P) = g_\chi^2 \int \frac{d^4 Q}{(2\pi)^4} 2\pi \delta((P-Q)^2 - m_\chi^2) \times \theta((P-Q)_0) \gamma^\mu (\not{P} - \not{Q} + m_\chi) \gamma^\nu D_{\mu\nu}^>(Q) \quad (\text{A2})$$

Writing $P = (E, p)$, the fermion's interaction rate is given by [76]

$$\Gamma = \frac{1}{4E} \text{tr} [(\not{P} + m_\chi) \Sigma^>(P)] \quad (\text{A3})$$

Evaluating the Dirac trace, we have

$$\text{tr} [(\not{P} + m_\chi) \gamma^\mu (\not{P} - \not{Q} + m_\chi) \gamma^\nu] = 4(P \cdot Q \eta^{\mu\nu} + P^\mu (P-Q)^\nu + P^\nu (P-Q)^\mu) \quad (\text{A4})$$

Assuming that the mediator couples weakly to the SM medium, the dominant contribution to $\Sigma^>$ comes from having only SM states in the shaded circle. In this case, we have (to leading order in the SM-mediator coupling) [76]

$$D_{\mu\nu}^>(Q) = D_{\mu\nu}^{>F}(Q) - \frac{2}{(Q^2 - m_\chi^2)^2} \text{sgn}(q_0) (1 + f(q_0)) \text{Im} \Pi_{\mu\nu}(Q) \quad (\text{A5})$$

where $Q = (q_0, q)$, $D_{\mu\nu}^{>F}(Q)$ is the free cut propagator, $f(E) \equiv (e^{E/T} - 1)^{-1}$ is the bosonic thermal occupation number for the temperature T of the medium, and $\Pi_{\mu\nu}(Q)$ is the mediator's in-medium self-energy. The real part of $\Pi_{\mu\nu}$ does not contribute, since the integral for $\Sigma^>$ only receives contributions from $Q^2 < 0$, where the mediator is always off-shell. Going forwards, we will assume that the temperature of our medium is negligible, so we can neglect the $f(q_0)$ term.

Using the fact that $Q_\mu \Pi^{\mu\nu}(Q) = 0$ (which holds if the current we couple to is conserved), we can write

$$\Gamma = \frac{2g_\chi^2}{E} \int \frac{d^3 q}{(2\pi)^3} \frac{1}{2E'} \frac{1}{(Q^2 - m_\chi^2)^2} \times (-\text{Im} \Pi_{\mu\nu}(Q)) \left(\frac{Q^2}{2} \eta^{\mu\nu} + 2P^\mu P^\nu \right) \quad (\text{A6})$$

where $Q_\mu = (q_0, q)$ is such that $P - Q$ is on-shell. Here, since we are assuming negligible medium temperature, we integrate over q such that $q_0 \geq 0$ (as upscattering cannot occur).

So far, our calculation has been fully relativistic. If the incoming DM is non-relativistic in the rest frame of the medium, so $P \simeq m_\chi(1 + v_\chi^2/2, v_\chi)$, then the only part of the $\frac{Q^2}{2} \eta^{\mu\nu} + 2P^\mu P^\nu$ term in Eq. (A6) that is not suppressed for $v_\chi \ll 1$ is the 00 component, which is $\simeq 2m_\chi^2$. This picks out the longitudinal part Π_L of $\Pi_{\mu\nu}$, since $\Pi_{00} = \frac{q^2}{Q^2} \Pi_L$ (note that our convention differs from that of [76], which takes $\Pi_L = \Pi_{00}$). As we will show below (in Section A 1 a), considering only the $\text{Im} \Pi_{00}$ term gives the leading contribution for $v_\chi \ll 1$, with

$$\Gamma \simeq 2g_\chi^2 \int \frac{d^3 q}{(2\pi)^3} \frac{1}{(q^2 + m_\chi^2)^2} (-\text{Im} \Pi_L(q_0, q)) \quad (\text{A7})$$

since $q_0 \ll q$.

Specialising to a dark photon mediator with kinetic mixing κ , we have

$$\text{Im} \Pi_{\mu\nu}(Q) = \kappa^2 Q^4 \text{Im}(-iD_{\mu\nu}(Q)) \quad (\text{A8})$$

where $D_{\mu\nu}$ is the in-medium propagator for the SM photon, in Lorenz gauge (for more details, see Appendix D of [45]). The longitudinal dielectric function is related to the longitudinal part D_L (defined via $D_{\mu\nu} = -iD_L P_{\mu\nu}^L + \dots$, where $P_{\mu\nu}^L$ is the longitudinal projector) as $\epsilon_L^{-1}(Q) = -Q^2 D_L(Q)$ [77], so we can write the DM scattering rate as

$$\Gamma \simeq 2g_\chi^2 \kappa^2 \int \frac{d^3 q}{(2\pi)^3} \frac{q^2}{(q^2 + m_\chi^2)^2} \text{Im} \left(\frac{-1}{\epsilon_L(\omega_q, q)} \right) \quad (\text{A9})$$

where ω_q puts the DM particle on-shell, in agreement with Eq. (2).

a. Sub-leading contributions

In the $\frac{Q^2}{2} \eta^{\mu\nu} + 2P^\mu P^\nu$ expression, terms other than the 00 component are suppressed by powers of $v_\chi \ll 1$. However, if $\text{Im} \Pi_{\mu\nu}(Q)$ could be much larger for these other components, then they could still be important. For example, we might worry that, since the exchange of a transverse photon is unscreened for small q_0 , whereas longitudinal exchange is screened [76], transverse contributions might become important. However, for the case

of a dark photon mediator, $D_{\mu\nu}$ obeys additional sum rules which mean that the velocity-averaged scattering rate is dominated by the longitudinal-exchange expression in Eq. (A7) above, as we show here.

If $J_\mu = J_\mu^{(0)} e^{iQ \cdot x}$ is a charge density perturbation with wavevector Q_μ , then the medium's EM field response is given by $A_\mu = -iD_{\mu\nu}^R(Q)J^\nu$, where $D_{\mu\nu}^R$ is the retarded in-medium propagator for the photon. Consequently, writing $R_{\mu\nu} \equiv iD_{\mu\nu}^R$, the time-averaged power extracted from the charge perturbation is set by $iq_0 J_\mu^* A^\mu + \text{h.c.} = q_0 (J^\mu)^* J^\nu \text{Im } R_{\mu\nu}$. If the medium is in its ground state, then this power should be positive for any perturbing current — that is, the medium should absorb energy from the perturbation, rather than emitting energy. Current conservation $\partial_\mu J^\mu = 0$ implies that $Q_\mu J^\mu = 0$, so for any vector ϵ^μ perpendicular to Q_μ , we should have that $(\epsilon^\mu)^* \epsilon^\nu \text{Im } R_{\mu\nu} \geq 0$.

At high enough frequencies, corresponding to timescales much faster than the response times of the system's matter, the response function should be almost equal to that in vacuum. If we fix the spatial vector q , then for the spatial directions transverse to q , the response function at large q_0 will be $R_{ij} \simeq -\frac{\delta_{ij}}{q_0^2}$. Consequently, the Kramers-Kronig relations give

$$R_{ij}(0, q) = \frac{2}{\pi} \int_0^\infty \frac{dq_0}{q_0} \text{Im } R_{ij}(q_0, q) \quad (\text{A10})$$

This equation is not immediately useful as a sum rule, since the integrand may not always be non-negative. However, if we take $q = (0, 0, q)$ (without loss of generality), then $\text{Im } R_{11}$ and $\text{Im } R_{22}$ correspond to $(\epsilon^\mu)^* \epsilon^\nu \text{Im } R_{\mu\nu}$ for a spatial vector ϵ_μ which is perpendicular to Q_μ for all q_0 , so are always positive. Consequently, we have

$$R_{11}(0, q) = \frac{2}{\pi} \int_0^\infty \frac{dq_0}{q_0} \text{Im } R_{11}(q_0, q) \quad (\text{A11})$$

where the integrand is always positive, and similarly for R_{22} , giving us sum rules for the transverse components of the propagator.

If we are interested in the v_χ -averaged scattering rate, for an isotropic v_χ distribution, then the appropriate integrand arising from Eq. (A6) is

$$\left\langle \frac{Q^2}{2} \eta^{\mu\nu} \text{Im } R_{\mu\nu} + 2P_0^2 \text{Im } R_{00} - 4P_0 P_3 \text{Im } R_{03} + 2P_3^2 \text{Im } R_{33} + 2P_1^2 \text{Im } R_{11} + 2P_2^2 \text{Im } R_{22} \right\rangle \quad (\text{A12})$$

where the angle brackets denote averaging over v_χ . The contributions from the $\text{Im } R_{11}, \text{Im } R_{22}$ terms can be bounded using the sum rule from Eq. (A11). The $\text{Im } R_{03}, \text{Im } R_{33}$ terms can be related to ϵ_L^{-1} , so can be bounded using the sum rule from Eq. (4). Doing so, we

find that all of the other terms have v_χ -suppressed contributions compared to $2P_0^2 \text{Im } R_{00}$, which gives rise to Eq. (A9).

If we are interested in the v_χ -averaged scattering rate, for an isotropic v_χ distribution, then the appropriate integrand arising from Eq. (A6) is

$$\left\langle \frac{Q^2}{2} \eta^{\mu\nu} \text{Im } D_{\mu\nu} + 2P_0^2 \text{Im } D_{00} - 4P_0 P_3 \text{Im } D_{03} + 2P_3^2 \text{Im } D_{33} + 2P_1^2 \text{Im } D_{11} + 2P_2^2 \text{Im } D_{22} \right\rangle \quad (\text{A13})$$

where the angle brackets denote averaging over v_χ (the use of the retarded propagator does not make a difference here). The contributions from the $\text{Im } D_{11}, \text{Im } D_{22}$ terms can be bounded using the sum rule from Eq. (A11). The $\text{Im } D_{03}, \text{Im } D_{33}$ terms can be related to ϵ_L^{-1} , so can be bounded using the sum rule from Eq. (4). Doing so, we find that all of the other terms have v_χ -suppressed contributions compared to $2P_0^2 \text{Im } D_{00}$, which gives rise to Eq. (A9).

2. Scalar mediator

For a scalar mediator ϕ , we have

$$\Sigma^>(P) = g_\chi^2 \int \frac{d^4 Q}{(2\pi)^4} 2\pi\delta((P-Q)^2 - m_\chi^2) \quad (\text{A14})$$

$$\times \theta((P-Q)_0)(\not{P} - \not{Q} + m_\chi) D^>(Q) \quad (\text{A15})$$

and

$$D^>(Q) = D^{>F}(Q) - \frac{2}{(Q^2 - m_\phi^2)^2} \text{sgn}(q_0)(1 + f(q_0)) \text{Im } \Pi(Q) \quad (\text{A16})$$

where $\Pi(Q)$ is the mediator's in-medium self-energy. Evaluating the Dirac trace for the scattering rate,

$$\text{tr}[(\not{P} + m_\chi)(\not{P} - \not{Q} + m_\chi)] = 4(2m_\chi^2 - P \cdot Q) \quad (\text{A17})$$

For a non-relativistic P , this is the same, to leading order, as the leading $\mu = \nu = 0$ component of the vector mediator's trace, so we have

$$\Gamma \simeq -2g_\chi^2 \int \frac{d^3 q}{(2\pi)^3} \frac{1}{(q^2 + m_\phi^2)^2} \text{Im } \Pi(q_0, q) \quad (\text{A18})$$

If ϕ couples with opposite strength to electrons and protons, then to leading order in the velocities of the electrons and protons, $\text{Im } \Pi$ is the same as the $\text{Im } \Pi_L$ expression for a vector mediator.

We would obtain similar expressions if we considered scalar DM. Compared to the non-relativistic calculations in [24, 25], which were spin-agnostic by construction, our calculations illustrate how to incorporate relativistic corrections, as well as mediators with different couplings.

Appendix B: DM velocity distribution

The DM scattering rate in an experiment will depend on the DM velocity distribution at Earth. While we do not have precise measurements of this distribution, a common model assumed in the direct detection literature is the truncated Maxwell-Boltzmann distribution [78, 79]. Writing v as the velocity relative to Earth, the DM velocity distribution is taken to be

$$f(v) = \frac{1}{N_0} e^{-(v+v_e)^2/v_0^2} \Theta(v_{\text{esc}} - |v + v_e|) \quad (\text{B1})$$

For the truncated Maxwell-Boltzmann distribution, we have

$$p_1(v_z) = \begin{cases} \frac{\pi^{3/2} v_0^3}{4v_e N_0} \left(\text{erf} \left(\frac{v_e - v_z}{v_0} \right) + \text{erf} \left(\frac{v_e + v_z}{v_0} \right) \right) - \frac{\pi v_0^2}{N_0} e^{-v_{\text{esc}}^2/v_0^2} & v_z < v_{\text{esc}} - v_e \\ \frac{\pi^{3/2} v_0^3}{4v_e N_0} \left(\text{erf} \left(\frac{v_{\text{esc}}}{v_0} \right) + \text{erf} \left(\frac{v_e - v_z}{v_0} \right) \right) - \frac{\pi v_0^2}{2N_0} \frac{v_e + v_{\text{esc}} - v_z}{v_e} e^{-v_{\text{esc}}^2/v_0^2} & v_z < v_{\text{esc}} + v_e \\ 0 & v_z > v_{\text{esc}} + v_e \end{cases} \quad (\text{B5})$$

Figure 10 plots $p_1(v_z)$ for the standard parameter values, illustrating that the difference between the truncated and non-truncated Maxwell-Boltzmann distributions is only important at high velocities, and correspondingly small p_1 values.

Appendix C: Other EM sum rules

As well as the $\int \frac{d\omega}{\omega} \text{Im}(-1/\epsilon_L(\omega))$ sum rule, there are also other constraints that the longitudinal dielectric function should satisfy [27, 28]. For example, suppose that $\epsilon(\omega) \simeq 1 - \omega_p^2/\omega^2$ for large enough $|\omega|$. Then, from the Kramers-Kronig relations,

$$\int_0^\infty d\omega \omega \text{Im} \left(\frac{-1}{\epsilon_L(\omega, k)} \right) = \frac{\pi}{2} \omega_p^2 \quad (\text{C1})$$

where

$$N_0 = \pi^{3/2} v_0^2 \left[v_0 \text{erf} \left(\frac{v_{\text{esc}}}{v_0} \right) - \frac{2v_{\text{esc}}}{\sqrt{\pi}} \exp \left(\frac{-v_{\text{esc}}^2}{v_0^2} \right) \right] \quad (\text{B2})$$

Standard values taken for these parameters are $v_0 \simeq 230 \text{ km s}^{-1}$, $v_e \simeq 240 \text{ km s}^{-1}$, $v_{\text{esc}} \simeq 600 \text{ km s}^{-1}$ [16].

In the $v_{\text{esc}} \rightarrow \infty$ limit (corresponding to a simple Maxwell-Boltzmann distribution in the Galactic frame, which can be useful for seeing the basic form of expressions), we have $N_0 = \pi^{3/2} v_0^3$. From Section II B, a useful quantity for computing DM scattering rates is

$$p_1(v_z) = \int dv_x dv_y \frac{d\Omega_e}{4\pi} f(v) \quad (\text{B3})$$

For a Maxwell-Boltzmann distribution, this is

$$p_1(v_z) = \frac{1}{4v_e} \left(\text{erf} \left(\frac{v_e - v_z}{v_0} \right) + \text{erf} \left(\frac{v_e + v_z}{v_0} \right) \right) \quad (\text{B4})$$

The $d\omega/\omega$ sum rule (Eq. (1)) can be viewed as corresponding to energy absorption from a delta-function pulse in time. In contrast, the $d\omega \omega$ sum rule from Eq. (C1) corresponds to energy absorption from a second-derivative-of-delta-function pulse (a rapid down-up-down sequence). This emphasises absorption at higher frequencies. Physically, since we are interested in low-mass DM absorption, and correspondingly, in smaller energy transfers, the $d\omega/\omega$ sum rule will be more useful for our purposes.

-
- [1] M. Schumann, *J. Phys. G* **46**, 103003 (2019), [arXiv:1903.03026 \[astro-ph.CO\]](#).
 - [2] B. W. Lee and S. Weinberg, *Physical Review Letters* **39**, 165 (1977).
 - [3] C. Boehm and P. Fayet, *Nuclear Physics B* **683**, 219 (2004).
 - [4] J. H. Chang, R. Essig, and A. Reinert, *Journal of High Energy Physics* **2021** (2021), [10.1007/jhep03\(2021\)141](#).
 - [5] C. Dvorkin, T. Lin, and K. Schutz, *Physical Review D* **99** (2019), [10.1103/physrevd.99.115009](#).
 - [6] L. J. Hall, K. Jedamzik, J. March-Russell, and S. M. West, *Journal of High Energy Physics* **2010** (2010), [10.1007/jhep03\(2010\)080](#).
 - [7] R. Essig, J. Mardon, and T. Volansky, *Phys. Rev. D* **85**, 076007 (2012), [arXiv:1108.5383 \[hep-ph\]](#).
 - [8] R. Essig, A. Manalaysay, J. Mardon, P. Sorensen, and T. Volansky, *Phys. Rev. Lett.* **109**, 021301 (2012), [arXiv:1206.2644 \[astro-ph.CO\]](#).
 - [9] R. Essig, M. Fernandez-Serra, J. Mardon, A. Soto, T. Volansky, and T.-T. Yu, *JHEP* **05**, 046 (2016), [arXiv:1509.01598 \[hep-ph\]](#).

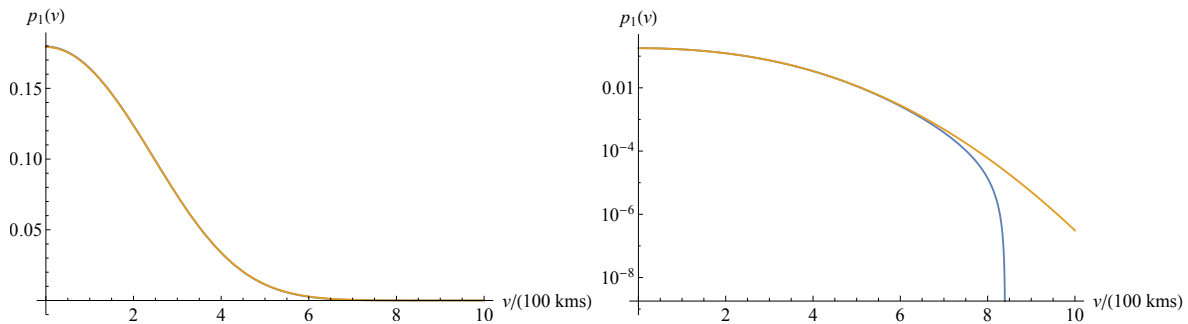


FIG. 10. Direction-averaged velocity distribution at Earth for the truncated Maxwell-Boltzmann DM velocity distribution from Appendix B. The blue curve shows the distribution for $v_{\text{esc}} = 600 \text{ km s}^{-1}$, and the orange curve for $v_{\text{esc}} \rightarrow \infty$. The difference between these curves is not visible in the linear-scale plot in the left panel, only in the log-scale plot in the right panel.

- [10] Y. Hochberg, Y. Zhao, and K. M. Zurek, *Phys. Rev. Lett.* **116**, 011301 (2016), arXiv:1504.07237 [hep-ph].
- [11] Y. Hochberg, M. Pyle, Y. Zhao, and K. M. Zurek, *JHEP* **08**, 057 (2016), arXiv:1512.04533 [hep-ph].
- [12] Y. Hochberg, Y. Kahn, M. Lisanti, C. G. Tully, and K. M. Zurek, *Phys. Lett. B* **772**, 239 (2017), arXiv:1606.08849 [hep-ph].
- [13] Y. Hochberg, Y. Kahn, M. Lisanti, K. M. Zurek, A. G. Grushin, R. Ilan, S. M. Griffin, Z.-F. Liu, S. F. Weber, and J. B. Neaton, *Phys. Rev. D* **97**, 015004 (2018), arXiv:1708.08929 [hep-ph].
- [14] S. Derenzo, R. Essig, A. Massari, A. Soto, and T.-T. Yu, *Phys. Rev. D* **96**, 016026 (2017), arXiv:1607.01009 [hep-ph].
- [15] N. A. Kurinsky, T. C. Yu, Y. Hochberg, and B. Cabrera, *Phys. Rev. D* **99**, 123005 (2019), arXiv:1901.07569 [hep-ex].
- [16] S. M. Griffin, K. Inzani, T. Trickle, Z. Zhang, and K. M. Zurek, *Phys. Rev. D* **101**, 055004 (2020).
- [17] C. Blanco, J. I. Collar, Y. Kahn, and B. Lillard, *Phys. Rev. D* **101**, 056001 (2020), arXiv:1912.02822 [hep-ph].
- [18] T. Trickle, Z. Zhang, K. M. Zurek, K. Inzani, and S. Griffin, *JHEP* **03**, 036 (2020), arXiv:1910.08092 [hep-ph].
- [19] R. M. Geilhufe, F. Kahlhoefer, and M. W. Winkler, *Physical Review D* **101** (2020), 10.1103/physrevd.101.055005.
- [20] Y. Hochberg, I. Charaev, S.-W. Nam, V. Verma, M. Colangelo, and K. K. Berggren, *Phys. Rev. Lett.* **123**, 151802 (2019), arXiv:1903.05101 [hep-ph].
- [21] A. Coskuner, A. Mitridate, A. Olivares, and K. M. Zurek, *Physical Review D* **103** (2021), 10.1103/physrevd.103.016006.
- [22] S. M. Griffin, Y. Hochberg, K. Inzani, N. Kurinsky, T. Lin, and T. C. Yu, *Phys. Rev. D* **103**, 075002 (2021), arXiv:2008.08560 [hep-ph].
- [23] S. Knapen, T. Lin, and K. M. Zurek, *Phys. Rev. D* **96**, 115021 (2017), arXiv:1709.07882 [hep-ph].
- [24] Y. Hochberg, Y. Kahn, N. Kurinsky, B. V. Lehmann, T. C. Yu, and K. K. Berggren, *Phys. Rev. Lett.* **127**, 151802 (2021), arXiv:2101.08263 [hep-ph].
- [25] S. Knapen, J. Kozaczuk, and T. Lin, *Physical Review D* **104** (2021), 10.1103/physrevd.104.015031.
- [26] P. Nozières and D. Pines, *Phys. Rev.* **113**, 1254 (1959).
- [27] G. D. Mahan, *Many-Particle Physics* (Springer, Boston, MA, 2000).
- [28] M. Dressel and G. Grüner, *Electrodynamics of Solids* (Cambridge University Press, 2002).
- [29] J. Dreyling-Eschweiler (ALPS-II), in *Proceedings, 10th Patras Workshop on Axions, WIMPs and WISPs (AXION-WIMP 2014): Geneva, Switzerland, June 29-July 4, 2014* (2014) pp. 63–66, arXiv:1409.6992 [physics.ins-det].
- [30] J. Dreyling-Eschweiler, N. Bastidon, B. Döbrich, D. Horns, F. Januschek, and A. Lindner, *J. Mod. Opt.* **62**, 1132 (2015), arXiv:1502.07878 [physics.ins-det].
- [31] B. Cabrera, R. M. Clarke, P. Colling, A. J. Miller, S. Nam, and R. W. Romani, *Applied Physics Letters* **73**, 735 (1998), <https://doi.org/10.1063/1.121984>.
- [32] B. S. Karasik, S. V. Pereverzev, A. Soibel, D. F. Santavicca, D. E. Prober, D. Olaya, and M. E. Gershenson, *Appl. Phys. Lett.* **101**, 052601 (2012), arXiv:1207.2164 [physics.ins-det].
- [33] A. E. Lita, A. J. Miller, and S. W. Nam, *Opt. Express* **16**, 3032 (2008).
- [34] N. Bastidon, D. Horns, and A. Lindner (2015) arXiv:1509.02064 [physics.ins-det].
- [35] B. A. Mazin, in *American Institute of Physics Conference Series*, American Institute of Physics Conference Series, Vol. 1185, edited by B. Young, B. Cabrera, and A. Miller (2009) pp. 135–142.
- [36] P. Day, H. Leduc, B. A. Mazin, A. Vayonakis, and J. Zmuidzinas, *Nature*, **425**, 817 (2003).
- [37] J. Gao, M. R. Vissers, M. O. Sandberg, F. C. S. da Silva, S. W. Nam, D. P. Pappas, D. S. Wisbey, E. C. Langman, S. R. Meeker, B. A. Mazin, H. G. Leduc, J. Zmuidzinas, and K. D. Irwin, *Applied Physics Letters* **101**, 142602 (2012), <https://doi.org/10.1063/1.4756916>.
- [38] K. M. Rosfjord, J. K. W. Yang, E. A. Dauler, A. J. Kerman, V. Anant, B. M. Voronov, G. N. Gol'tsman, and K. K. Berggren, *Opt. Express* **14**, 527 (2006).
- [39] D. V. Reddy, R. R. Nerem, S. W. Nam, R. P. Mirin, and V. B. Verma, *Optica* **7**, 1649 (2020).
- [40] V. B. Verma *et al.*, “Single-photon detection in the mid-infrared up to 10 micron wavelength using tungsten silicide superconducting nanowire detectors,” (2020), arXiv:2012.09979 [physics.ins-det].
- [41] E. E. Wollman *et al.*, *Opt. Express* **25**, 26792 (2017).
- [42] Y. Hochberg, B. Lehmann, I. Charaev, J. Chiles, S.-W. Nam, and K. K. Berggren, (2021), arXiv:2110.01586 [hep-ph].

- [43] P. C. Bunting, G. Gratta, T. Melia, and S. Rajendran, *Phys. Rev. D* **95**, 095001 (2017), [arXiv:1701.06566 \[hep-ph\]](#).
- [44] O. V. Dolgov, D. A. Kirzhnits, and E. G. Maksimov, *Reviews of Modern Physics* **53**, 81 (1981).
- [45] W. DeRocco, M. Galanis, and R. Lasenby, (2022), [arXiv:2201.05167 \[hep-ph\]](#).
- [46] D. Carney, H. Häffner, D. C. Moore, and J. M. Taylor, (2021), [arXiv:2104.05737 \[quant-ph\]](#).
- [47] D. Budker, P. W. Graham, H. Ramani, F. Schmidt-Kaler, C. Smorra, and S. Ulmer, (2021), [arXiv:2108.05283 \[hep-ph\]](#).
- [48] Y. Sun, H. Xu, B. Da, S.-f. Mao, and Z.-j. Ding, *Chinese Journal of Chemical Physics* **29**, 663 (2016), <https://doi.org/10.1063/1674-0068/29/cjcp1605110>.
- [49] S. Knapen, J. Kozaczuk, and T. Lin, (2021), [arXiv:2104.12786 \[hep-ph\]](#).
- [50] A. Coskuner, T. Trickle, Z. Zhang, and K. M. Zurek, (2021), [arXiv:2102.09567 \[hep-ph\]](#).
- [51] S. Knapen, T. Lin, M. Pyle, and K. M. Zurek, *Phys. Lett. B* **785**, 386 (2018), [arXiv:1712.06598 \[hep-ph\]](#).
- [52] S. Griffin, S. Knapen, T. Lin, and K. M. Zurek, *Phys. Rev. D* **98**, 115034 (2018), [arXiv:1807.10291 \[hep-ph\]](#).
- [53] T. Trickle and Z. Zhang, personal communication.
- [54] G. B. Gelmini, V. Takhistov, and E. Vitagliano, *Phys. Lett. B* **809**, 135779 (2020), [arXiv:2006.13909 \[hep-ph\]](#).
- [55] A. Fasolino, M. Parrinello, and M. Tosi, *Physics Letters A* **66**, 119 (1978).
- [56] R. M. Geilhufe, B. Olsthoorn, A. D. Ferella, T. Koski, F. Kahlhoefer, J. Conrad, and A. V. Balatsky, *physica status solidi (RRL) - Rapid Research Letters* **12**, 1800293 (2018).
- [57] S. A. Knickerbocker and A. K. Kulkarni, *Journal of Vacuum Science & Technology A: Vacuum, Surfaces, and Films* **14**, 757 (1996).
- [58] I. Bozovic, *Physical Review B* **42**, 1969 (1990).
- [59] N. D. Kuz'michev and G. P. Motulevich, "Determination of the electron characteristics of niobium nitride by an optical method," (1983).
- [60] W. Cai and V. Shalaev, *Optical Metamaterials* (Springer New York, 2010).
- [61] N. Maleeva, L. Grünhaupt, T. Klein, F. Levy-Bertrand, O. Dupre, M. Calvo, F. Valenti, P. Winkel, F. Friedrich, W. Wernsdorfer, A. V. Ustinov, H. Rotzinger, A. Monfardini, M. V. Fistul, and I. M. Pop, *Nature Communications* **9** (2018), [10.1038/s41467-018-06386-9](https://doi.org/10.1038/s41467-018-06386-9).
- [62] H. Vogel and J. Redondo, *Journal of Cosmology and Astroparticle Physics* **2014**, 029 (2014).
- [63] J. H. Chang, R. Essig, and S. D. McDermott, *Journal of High Energy Physics* **2018** (2018), [10.1007/jhep09\(2018\)051](https://doi.org/10.1007/jhep09(2018)051).
- [64] R. Essig, A. Manalaysay, J. Mardon, P. Sorensen, and T. Volansky, *Physical Review Letters* **109** (2012), [10.1103/physrevlett.109.021301](https://doi.org/10.1103/physrevlett.109.021301).
- [65] R. Essig, T. Volansky, and T.-T. Yu, *Physical Review D* **96** (2017), [10.1103/physrevd.96.043017](https://doi.org/10.1103/physrevd.96.043017).
- [66] D. I. Yakubovsky, A. V. Arsenin, Y. V. Stebunov, D. Y. Fedyanin, and V. S. Volkov, *Optics Express* **25**, 25574 (2017).
- [67] J. Chiles, I. Charaev, R. Lasenby, M. Baryakhtar, J. Huang, A. Roshko, G. Burton, M. Colangelo, K. Van Tilburg, A. Arvanitaki, S.-W. Nam, and K. K. Berggren, (2021), [arXiv:2110.01582 \[hep-ex\]](#).
- [68] T. Polakovic, W. Armstrong, G. Karapetrov, Z.-E. Meziani, and V. Novosad, *Nanomaterials* **10**, 1198 (2020).
- [69] S. Knapen, T. Lin, M. Pyle, and K. M. Zurek, *Physics Letters B* **785**, 386–390 (2018).
- [70] S. Griffin, S. Knapen, T. Lin, and K. M. Zurek, *Phys. Rev. D* **98**, 115034 (2018).
- [71] K. M. Rosfjord, J. K. W. Yang, E. A. Dauler, A. J. Kerman, V. Anant, B. M. Voronov, G. N. Gol'tsman, and K. K. Berggren, *Opt. Express* **14**, 527 (2006).
- [72] V. B. Verma, B. Korzh, A. B. Walter, A. E. Lita, R. M. Briggs, M. Colangelo, Y. Zhai, E. E. Wollman, A. D. Beyer, J. P. Allmaras, B. Bumble, H. Vora, D. Zhu, E. Schmidt, K. K. Berggren, R. P. Mirin, S. W. Nam, and M. D. Shaw, "Single-photon detection in the mid-infrared up to 10 micron wavelength using tungsten silicide superconducting nanowire detectors," (2020), [arXiv:2012.09979 \[physics.ins-det\]](#).
- [73] N. F. Bell, G. Busoni, S. Robles, and M. Virgato, *JCAP* **09**, 028 (2020), [arXiv:2004.14888 \[hep-ph\]](#).
- [74] N. F. Bell, G. Busoni, S. Robles, and M. Virgato, *JCAP* **03**, 086 (2021), [arXiv:2010.13257 \[hep-ph\]](#).
- [75] N. F. Bell, G. Busoni, M. E. Ramirez-Quezada, S. Robles, and M. Virgato, (2021), [arXiv:2104.14367 \[hep-ph\]](#).
- [76] M. L. Bellac, *Thermal Field Theory* (Cambridge University Press, 2011).
- [77] T. Altherr and U. Kraemmer, *Astroparticle Physics* **1**, 133 (1992).
- [78] C. McCabe, *Physical Review D* **82** (2010), [10.1103/physrevd.82.023530](https://doi.org/10.1103/physrevd.82.023530).
- [79] M. Lisanti, in *New Frontiers in Fields and Strings* (WORLD SCIENTIFIC, 2016).